ACS APPLIED MATERIALS & INTERFACES

Research Article

Cite This: ACS Appl. Mater. Interfaces 2018, 10, 42796−42803

www.acsami.org

Honeycomb-like Hard Carbon Derived from Pine Pollen as High-Performance Anode Material for Sodium-Ion Batteries

Yanjia Zhang,[†,§] Xue Li,[†,§] Peng Dong,[†] Gang Wu,[†] Jie Xiao,[†] Xiaoyuan Zeng,*[,†,‡] Yingjie Zhang,*[,†] and Xueliang Sun*[,‡]

[†]National and Local Joint Engineering Laboratory for Lithium-ion Batteries and Materials Preparation Technology, Key Laboratory of Advanced Battery Materials of Yunnan Province, Faculty of Metallurgical and Energy Engineering, Kunming University of Science and Technology, Kunming 650093, China

[‡]Department of Mechanical and Materials Engineering, University of Western Ontario, London N6A 5B9, Ontario, Canada

Supporting Information

ABSTRACT: Sodium-ion batteries are regarded as one of the most promising energy storage systems, but the choice of anode material is still facing great challenges. Biomass carbon materials were explored for their low cost and wide range of sources. Here, a hard carbon material with a "honeycomb" structure using pine pollen (PP) as a precursor was successfully prepared and applied as an anode. The initial discharge capacity can reach 370 mA h g^{-1} at a current density of 0.1 A g^{-1}. After cycling 200 times, the reversible capacity also stabled at 203.3 mA h g^{-1} with the retention rate of 98%. We further studied the sodium storage mechanism by different methods, especially the Na^+ diffusivity coefficient (D_{Na^+}) calculated by galvanostatic intermittent titration technique, which was more accurate. Interestingly, the trend of D_{Na^+} coincides with cyclic voltammetry curves. Carbonized PP exhibited excellent electrochemical properties because of its three-dimensional structure and larger layer spacing (~0.41 nm), which reduces the resistance of sodium ions to intercalation and deintercalation.

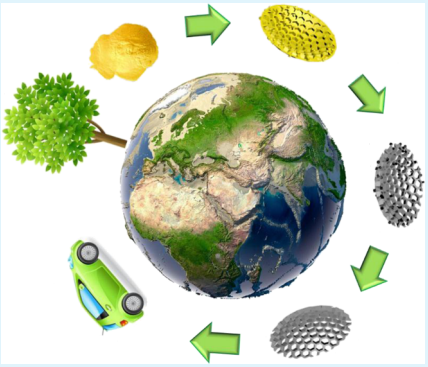

KEYWORDS: *energy storage, biomass-derived, hard carbon, anode, sodium-ion batteries*

INTRODUCTION

As the environmental crisis aggravated, the development of clean and recyclable systems of energy storage has become more urgent.[1−6] Lithium-ion batteries (LIBs) are widely utilized in energy storage systems, such as hydraulics, firepower, wind power, and solar power plants, because of their good cycle performance and high energy density.[7] However, with the increase of market demand, lithium metal has been insufficient for a long time, which leads to higher and higher prices, directly increasing the production cost of various lithium-based batteries.[8] In the long run, there is an urgent need to find a new storage system that rivals lithium-based batteries.[9−11] The sodium element is considered the most promising alternative to lithium based on their similar physicochemical properties, and the most attractive reason is that sodium is widely distributed and inexpensive.[12−16] The charge and discharge behavior of sodium-ion batteries (SIBs) is similar to that of LIBs, but the diameter of sodium ions is 0.204 nm, which is longer than lithium ions (0.152 nm).[17,18] The larger volume leads to a slow process of kinetics on sodium ions' insertion−extraction in the electrode material, causing a lower reversible capacity.[19,20] The key factor to solve this problem is to design an electrode material with larger layer spacing to store sodium ions.

Among a wide variety of electrode materials, carbon materials that benefit from low cost, high conductivity, stable physical and chemical properties are most widely used.[21−23] Structurally, the carbon materials used to store sodium fall into two broad categories: ordered soft carbon[21] and disordered hard carbon.[24,25] Soft carbon is so tightly packed that it gives sodium ions less access to the interior of the material, whereas hard carbon provides more channels. Biomass-derived carbon is mostly hard carbon with the widest variety of sources, diverse structures and topographies, as well as its own multiple elements that do not require postprocessing.[26−30] The use of biomass-derived carbon in the negative electrode of SIBs has made some progress.[31,32] For example, Wang[33] made peanut skin as a precursor, prepared hierarchical porous carbon with layer spacing of 0.37−0.39 nm; the first discharge capacity can be up to 1275 mA h g^{-1} at 100 mA g^{-1}, but the Coulomb efficiency is only 29%. Cao[34] successfully processed rapeseed seeds into carbon material, and the distance between layers was 0.39 nm, at 25 mA g^{-1}; the battery showed a discharge capacity of 237 mA h g^{-1} for the first cycle. Zhu[35] carbonized cherry into a honeycomb-like fold of carbon material in a high-

Received: August 2, 2018
Accepted: November 21, 2018
Published: November 21, 2018

DOI: 10.1021/acsami.8b13160
ACS Appl. Mater. Interfaces 2018, 10, 42796−42803

temperature pyrolysis method; the layer spacing can enlarge up to 0.44 nm, and the capacity retention after 100 cycles is still maintained at 99.3% at the current density of 20 mA g^{-1}. In addition, the hard carbon derived from banana peels,[36] apple biowaste,[37] and nature leaves[38] has also been studied as anode material.

In this paper, we successfully derived hard carbon material with "honeycomb" morphology using pine pollen (PP) as a precursor, with a specific surface area of 171.54 m^2 g^{-1} and a larger layer spacing of 0.41 nm. When carbonized PP (CPP) was applied as anode material of SIBs, the discharge capacity was still maintained at 203.7 mA h g^{-1} at 0.1 A g^{-1} after 200 cycles, and CPP also exhibited outstanding rate performance at 5 A g^{-1} with reversible capacity of 87 mA h g^{-1}. Besides the structural advantages, we carried out a detailed study of the sodium storage mechanism in CPP. First, the sodium storage mechanism was analyzed by cyclic voltammetry (CV). Studied by CV under different scan rates and D_{Na^+}, all the results prove that the reasoning is correct. What is more, the method by which we calculated D_{Na^+} is more accurate, and interestingly, the trend of sodium diffusion coefficient coincides with the CV curve. In conclusion, all the analyses of the sodium storage mechanism show that CPP is an excellent electrode material, and we believe that the outstanding performance of CPP can promote the application of biomass in SIBs. The synthesis process is shown in Figure 1, which contains the microstructure and application of CPP.

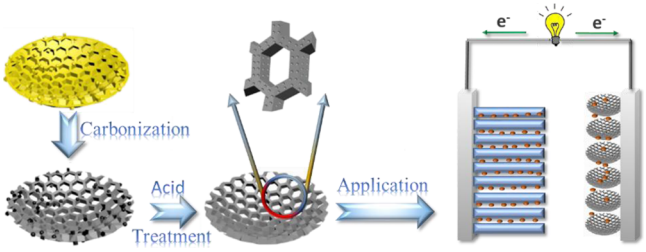

Figure 1. Preparation scheme of CPP.

EXPERIMENTAL SECTION

Synthesis of CPP. The preparation process of the CPP is described as follows: PP was carbonized at 900 °C for 1 h in argon atmosphere; the temperature increased at the rate of 5 °C min^{-1}. The obtained material was dissolved in 0.5 M sulfuric acid solution to remove the organic impurities. Finally, the product was washed to a neutral pH value, and dried overnight.

Material Characterization. The morphology of CPP was examined through scanning electron microscopy (TESCAN VEGA3, SEM) and transmission electron microscopy (Tecnai G2 F20 S-Twin, TEM). The composition and chemical state were measured by X-ray diffraction (Rigaku MiniFlex600 powder diffractometer, XRD), Raman spectroscopy (LabRAM HR Evolution), and PHI5000 Versaprobe-II spectrometer type X-ray photoelectron spectroscopy (XPS). The Brunauer–Emmett–Teller method was used to calculate the surface area, and CPP was first outgassed for 4 h at 150 °C under vacuum, then investigated on an automatic sorption analyzer (ASAP 2460) at 77 K according to the nitrogen adsorption–desorption process of pressure changes.

Electrochemical Measurements. The sodium-ion battery was assembled by using 2016-type coin cells. The anode electrode was prepared as follows. We mixed the CPP, Super P, and polyvinylidene-fluoride in *N*-methyl-2-pyrrolidone with a mass ratio of 8:1:1 to form a slurry. It was then spread onto a copper foil with the slurry thickness of 100 nm, and dried overnight at 120 °C. In order to make the material and copper foil bond better and closer, we polished the pole piece. Sodium metal was used as the cathode, separate cathode and anode with glass fiber (Whatman), and the electrolyte was 1 M $NaClO_4$ in a mixture solvent of ethylene carbonate/propylene carbonate (1:1). All the steps of battery assembly were carried out in an argon-protected glove box. Both the moisture and oxygen contents were under 0.1 ppm. At room temperature, we performed the charge–discharge performance on the testing system (CT2001A, LAND, China).

RESULTS AND DISCUSSION

The structure of CPP was studied by XRD patterns and Raman spectra. As Figure S1 demonstrates, two characteristic peaks of CPP are situated at $2\theta \approx 24°$ and 43°, which correspond to the (002) and (100) planes of carbon, showing that we successfully carbonized the CPP into a representative highly disordered hard carbon.[39] The value of L_c was calculated as 1.51 nm, which represented the layer thickness that along in the direction of *c*-axis between graphite microcrystalline. In addition, the empirical parameter *R* (2.03) suggests that our CPP contains just a few pieces of graphite sheets.[35] According to the literature,[36] the graphitization degree of CPP can reflect the capacity in storage sodium ions. On the basis of the analysis, we conducted a Raman test to further test the disorder degree. As Figure S2 shows, the spectra contain two prominent wide peaks at about 1343 (D band) and 1580 (G band) cm^{-1}, respectively. The peak ratio of I_D/I_G is 1.07, indicating that the CPP has an amorphous structure.

The N_2 adsorption–desorption isotherms of CPP are shown in Figure S3a, which belongs to the IV type isotherm,[40] inferring that the CPP was a mesoporous structure; this may be due to the gas generated during the carbonization process. On the basis of the classification of IUPAC, the relative pressure (P/P_0) ranging from 0.4 to 1.0 shows a typical H3-style hysteresis loop, indicating that the pores of CPP are disordered, which fits well with the TEM results. The distribution of pore size was acquired by using the Barrett–Joyner–Halenda (BJH) model, and the data were based on the adsorption branch to prevent the spurious peaks. Through the analysis of BET, the specific surface area of CPP is 171.54 m^2 g^{-1}. Simultaneously, the pore size of average is calculated as 4.82 nm. What is more, it can be seen from the inset figure in Figure S3b that most of the pores are spread at 2–4 nm, which is a favorable condition for storing sodium ions.[41]

The morphological characterization of CPP is shown in Figure 2. It is obvious that CPP shows a honeycomb-like structure (Figure 2a), and the surface of CPP has lots of irregular pores (Figure 2b), which is beneficial to store sodium ions. It can be observed from the high-resolution TEM graphic (Figure 2c) that CPP illustrates a representative hard carbon material construction, which contains unordered graphite microcrystals in a short distance, which contributes to the higher reversible specific capacity. We further confirmed the highly disordered microstructures by selected area electron diffraction (SAED) patterns (Figure 2c) with electron diffraction rings, and there were no diffraction spots on the dispersed diffraction rings, proving that CPP has the characteristics of hard carbon materials. As shown in Figure 2d, compared with graphite (0.335 nm),[19] the layer spacing of CPP (0.41 nm) is much bigger. The larger layer spacing promotes the transmission and storage of sodium ions, also improving the cycling stability. These results are supported by the XRD and Raman data.

DOI: 10.1021/acsami.8b13160
ACS Appl. Mater. Interfaces 2018, 10, 42796–42803

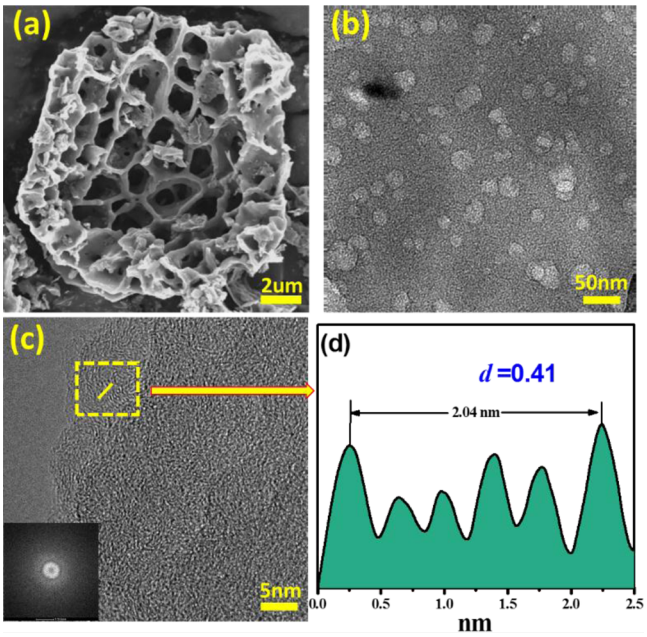

Figure 2. SEM (a) and TEM (b,c) images of PP with the SAED image in (c); (d) layer spacing of CPP along the direction of the yellow line segment.

The XPS survey spectrum is shown in Figure 3. From the full spectrum (Figure 3a), we can find that CPP primarily consists of C and O. In order to confirm the chemical condition of these two main elements, the high resolutions of C 1s and O 1s were fitted. Figure 3b displays three major characteristic peaks at 284.6, 285.4, and 287.2 eV, corresponding to the C−C, C−O, and C═O bonds, respectively. The C−C bond that basically exists in the nondefective graphite lattice has the highest peak area ratio of 57 at. %; then the C−O (26 at. %) and C═O (17 at. %) bonds lie in the defective graphite lattice. The characteristic peaks of the O 1s (Figure 3c) located in 530.9 and 532.4 eV correspond to the C═O and C−OH bonds, respectively.[42] According to the literature,[35,43] these functional groups that contain oxygen may contribute to the increased capacity because of the increased active site of the redox reaction on the CPP surface. In addition, Table S1 demonstrates the specific elements' percentage. It can be observed that our CPP also contains a small amount of nitrogen, which can promote the storage of sodium ions.

CV tests were conducted to investigate the storage process of sodium ions.[44] Figure 4a shows the first three laps taking 0.01−3 V as the electrochemical window at a sweep rate of 0.1 mV s^{-1}. There are three reduction peaks during the first discharge process; the obvious one near 0.95 V is mainly on account of the reaction between other functional groups and sodium ions, whereas the slight one near 0.13 V is likely due to the formation of a solid electrolyte interphase (SEI) layer. Notably, two reduction peaks vanished in the second and third cycles, demonstrating that the reactions that happened in the first cycle were irreversible, and well explained the low initial Coulombic efficiency of CPP. In addition, there is a pair of sharp redox peaks near 0.01 V, which indicates the insertion−extraction process of sodium ions in the mezzanine of graphitic microcrystallites. It can be seen that there is a large slope from 1 to 0.01 V, illustrating the adsorption process of sodium ions on the CPP surface, until the voltage turns to 0.01 V, the surface tends to be saturated, sodium ions primarily in the form of embedded, showing a sharp oxidation peak at low potential. All of these correspond to the oxidation process.

The discharge−charge profiles are shown in Figure 4b at 100 mA g^{-1}. The initial discharge and charge capacity can reach 370.1 and 221.5 mA h g^{-1}. However, the Coulombic efficiency is just 59.8%; this is basically due to the irreversible reactions on the surface of the material, which fits well with the CV results. Figure 4c studies the cyclability and Coulombic efficiency of CPP. At 200 mA g^{-1}, the CPP anode obtains a

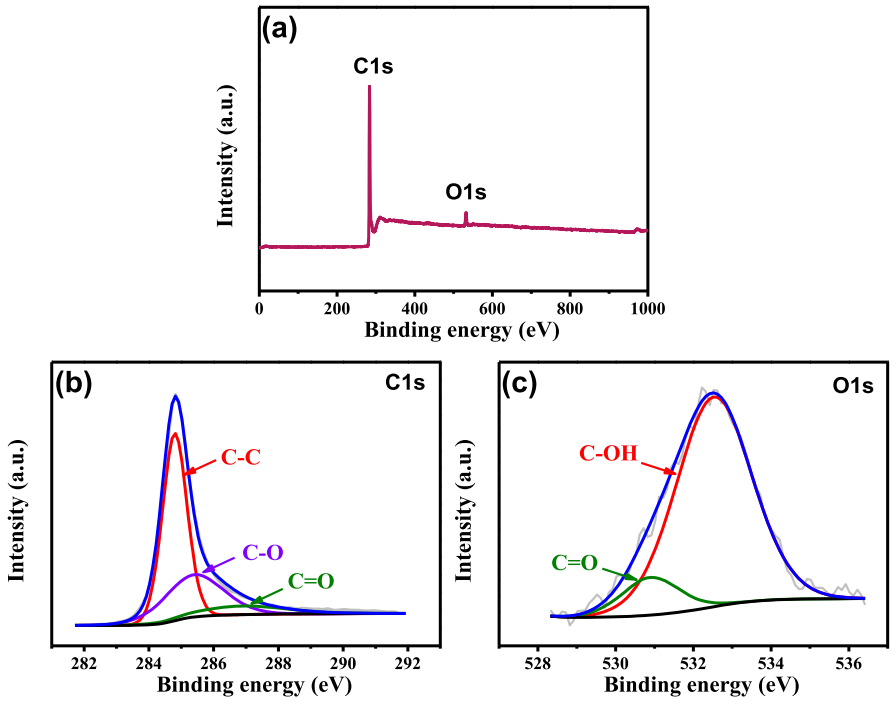

Figure 3. (a) XPS survey spectra of CPP specimens; high-resolution XPS C 1s spectra (b) and O 1s (c).

DOI: 10.1021/acsami.8b13160
ACS Appl. Mater. Interfaces 2018, 10, 42796−42803

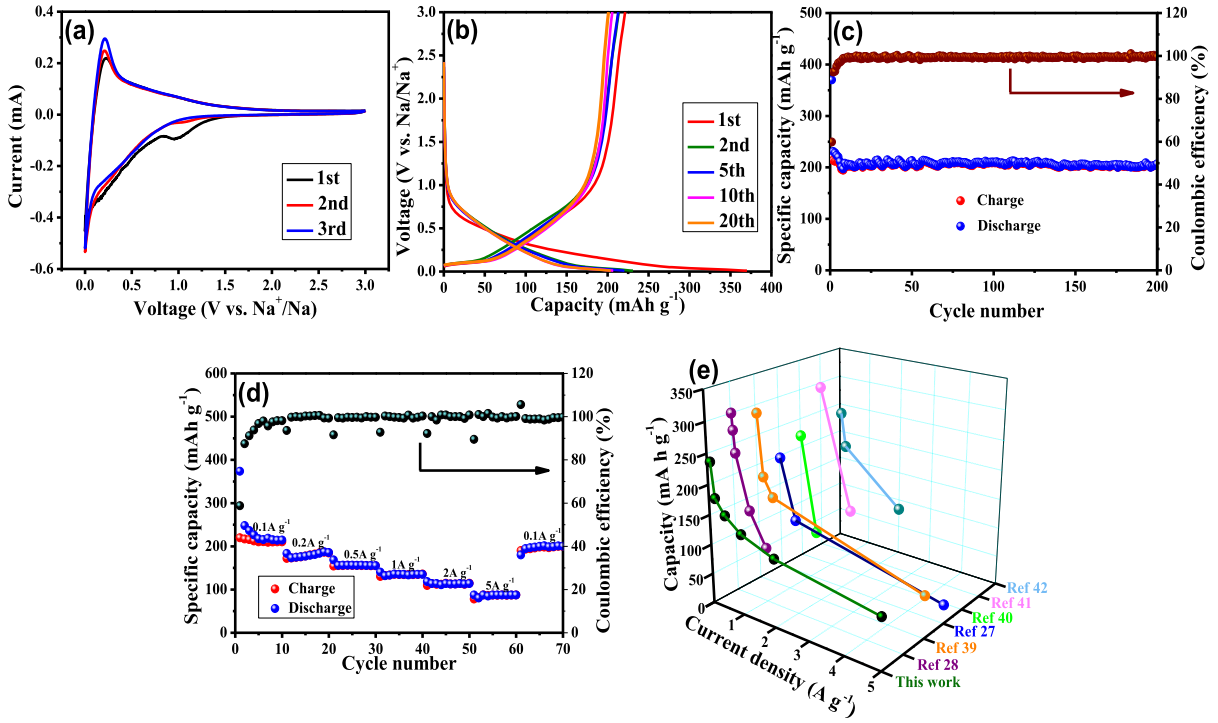

Figure 4. Electrochemical performance of CPP: (a) CV curves; (b) galvanostatic charge/discharge cycling profiles; (c) cycling performance at 100 mA g^{-1}; rate performance (d) and rate performance comparison of PP with the state-of-the-art in the literature (e).

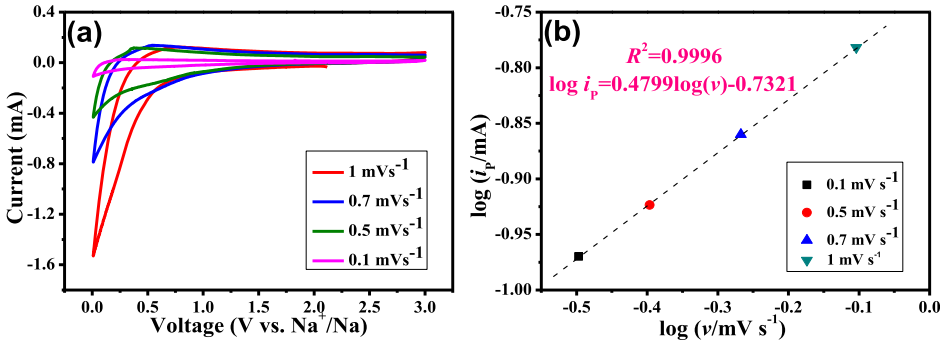

Figure 5. (a) CV curves for the CPP electrode between 0.1 and 3.0 V at different scan rates; (b) log(*ip*) vs log(*v*).

reversible capacity of 207.5 mA h g^{-1}. After 200 cycles, it still remained at 203.3 mA h g^{-1} with the retention rate of 98%, demonstrating high cycling stability. At the same time, we find that the discharge curve is mostly divided into two parts, one is the slope region and the other is the platform region,[45] which are located in the voltage of 1.2−0.1 and 0.1−0 V, respectively. Combined with the CV results, the slope section represents the adsorption process of sodium ions; the platform section refers to the insertion−extraction process. In order to ensure the superiority of the CPP electrode, we further tested the rate performance of CPP. As shown in Figure 4d, the CPP electrode presents average reversible capacities of 236.3, 192.8, 168.5, 140.3, 118.4, 87.3, and 201.4 mA h g^{-1} at the current rates of 100, 200, 500, 1000, 2000, 5000, and 100 mA g^{-1}, respectively. We are surprised that when it returns to 100 mA g^{-1}, the reversible capacity can reach 201.4 mA h g^{-1}, which is 85.2% of the initial value, indicating the stable structure and high reversible capacity during cycles. This phenomenon mainly benefits from the expanded graphite microcrystalline layer spacing, which is conducive to the transmission of sodium ions. We have also made some comparison about the rate performance among other biomass carbons in Figure 4e, CPP still outstanding at high current density.[34,35,46−49] More details can be seen in Table S2.

Figure S4 displays the Nyquist impedance plots of the sodium-ion battery with the CPP electrode for different cycles; the test was under the condition of 10^5 Hz to 10^{-2} Hz and scanning rates of 1 mV s^{-1}. All curves consist of a semicircular arc in the medium-high frequency section and a linear tail in the low section. As shown in Figure S4, the curves are fitted by the corresponding equivalent circuit, where R_s means the Ohmic contact resistance, R_{ct} correspond to charge transfer resistance, CPE means double-layer capacitance, and Z_w refers to the Warburg impedance of sodium ion diffusion.[50,51] Notably, R_{SEI} appearing after the first cycle represents the diffusion resistance caused by the SEI film.[52,53] As shown in Table S2, all curves are fitted with the error rate under 5%. It is obvious that both R_s and R_{ct} + R_{SEI} increase as the cycle progresses, but compared with R_s, the increment of R_{ct} + R_{SEI} decreases gradually, showing that the SEI film was obtained primarily in the first few cycles, which is consistent with the CV results.

DOI: 10.1021/acsami.8b13160
ACS Appl. Mater. Interfaces 2018, 10, 42796−42803

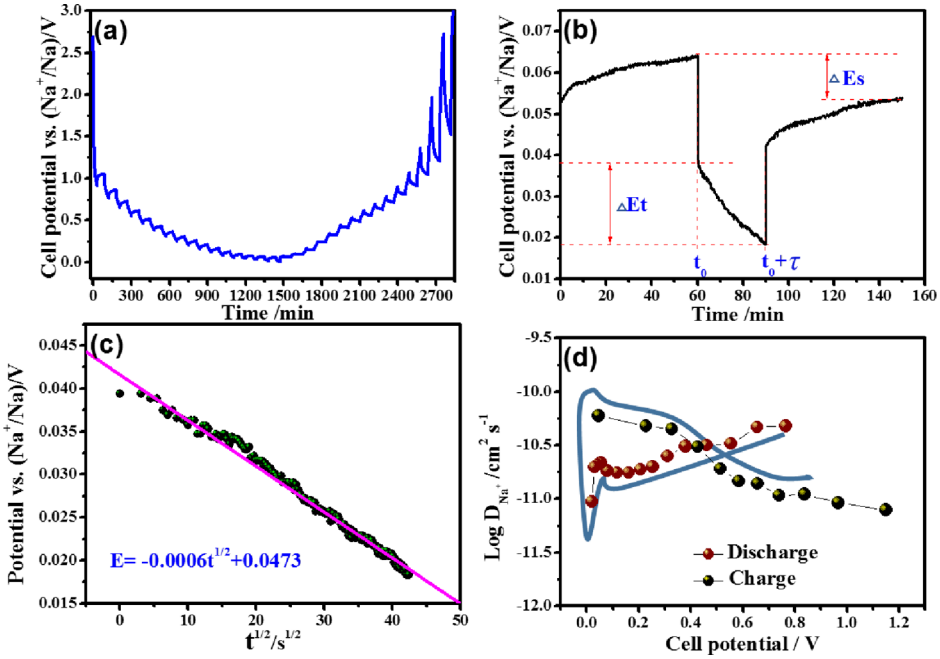

Figure 6. (a) GITT curve of CPP as electrode material; (b) single GITT titration curve; (c) linear fitting of discharge voltages E vs $\tau^{1/2}$ in a single GITT titration curve; (d) relationship between voltage and log DLi+ during the discharge and charge process.

As shown in Figure 5a, CV under several scan rates (0.1−1 mV s^{-1}) is a predominant way to further study the reaction mechanism. The relationship is as follows according to the formula[54]

$$i = avb$$

In this formula, i corresponds to the peak current, a and exponent b are adjustable values. Notably, b has two representative values. One value of b tends to be 0.5, indicating that semi-infinite diffusion controlled the current, whereas the other tends to be 1, demonstrating that the current is surface-controlled. From the CV curves, we can observe that the amount of sodium stored in the CPP is inversely proportional to the scan rates. The reason is that a high scan rate almost gives no time for sodium ions to diffuse.[55] We also find that as the scanning rate decreases, the potential difference ($\Delta E = |E_O - E_R|$) between the oxidation peak (E_O) and the reduction peak (E_R) gradually decreases, indicating that the CPP electrode is a reversible reaction, and can directly enhance the cycle ability of the sodium-ion battery. In order to obtain the value of b more intuitively, we converted the above formula, as shown in Figure 5b; the sweep rate satisfies the linear regression (R^2 = 0.9996), the b value 0.4799 represents the slope in the converted formula, very close to 0.5, as mentioned above, showing that semi-infinite diffusion mainly controls the current.[33,41,51] That fits well with the charge−discharge profiles, and gives a good explanation about the capacity obtained in the low-pressure area.

To reveal the excellent capability of CPP, the diffusivity coefficient of sodium ions (D_{Na^+}) was tested by galvanostatic intermittent titration technique (GITT) with a 0.2 C pulse current for 30 min between the rest gap for 1 h.[56−59] According to Fick's second law (reversal of reaction 1), the calculation formula is as follows

$$D_{Na^+} = \frac{4}{\pi}\left(\frac{m_B V_m}{M_B S}\right)^2 \left(\frac{\Delta E_s}{\tau(dE_\tau/d\sqrt{\tau})}\right)^2 \quad (1)$$

where m_B is the weight of CPP on the pole piece, V_m represents the molar volume of carbon, M_B represents the molecular mass of carbon, S represents the area of the active material on a single pole piece, τ represents the pulse time, ΔE_s represents the voltage difference at the time when the voltage reaches the steady state in a single GITT process, and L represents the thickness of the pole piece. In order to simplify the formula, Figure 6b shows a single GITT diagram, further comparing the relationship between voltage and $\tau^{1/2}$. As shown in Figure 6c, they satisfy the linear relationship. Therefore, the above formula can be simplified (reversal of reaction 2) as

$$D_{Na^+} = \frac{4}{\pi\tau}\left(\frac{m_B V_m}{M_B S}\right)^2 \left(\frac{\Delta E_s}{\Delta E_\tau}\right)^2 \quad (2)$$

As shown in Figure 6d, the D_{Na^+} was expressed in logarithmic form. With the depth of discharge, sodium ions that adsorbed on the surface of the electrode material of sodium ions gradually become saturated. Some of the sodium ions enter into the material through diffusion. However, because of the influence of external resistance, the kinetic process is slow, so the diffusion coefficient of the low-pressure region drops sharply. In the same way, a large number of sodium ions leave the surface at the beginning of the charge process, and the D_{Na^+} increased rapidly. With the reaction proceeding, the sodium ions on the surface became progressively lesser, so the sodium ions embedded in the intergranular graphite crystallites began to detach and the D_{Na^+} decreased. What is exciting is that the trend of D_{Na^+} in this paper coincides with the CV curve. This undoubtedly reaffirms our inference on the sodium storage mechanism of CPP. We attribute this to the more accurate calculation of the D_{Na^+}, different from the calculation method of previous reports; the parameter S here is the surface area of all the active materials on a single pole piece, not the contact area on the pole piece.[58,60]

DOI: 10.1021/acsami.8b13160
ACS Appl. Mater. Interfaces 2018, 10, 42796−42803

CONCLUSIONS

In this paper, the PP was used as precursor, and a hard carbon material with a honeycomb structure was successfully prepared. The application of CPP as the negative electrode showed excellent electrochemical performance. With the current density of 0.1 A g^{-1}, the capacity of discharge could reach 370.1 mA h g^{-1}; the initial Coulombic efficiency was 59.8%. CPP also exhibited superior cycling stability; the reversible capacity stabled at 203 mA h g^{-1} after 200 cycles and even had a high capacity of 87.3 mA h g^{-1} when it turned to 5 A g^{-1}, demonstrating better rate performance than other biomass carbon materials. On the basis of various electrochemical test data, it was concluded that the storage of sodium ion was mainly divided into two stages. The first stage was the high-voltage slope in the beginning of discharge; sodium ions during this period were basically adsorbed on the surface as the predominant form. When the sodium ion on the surface of the material tends to be saturated, sodium ions in the low voltage platform area mainly through the embedded form. In order to confirm this theory, we also tested the D_{Na^+}; the result was completely consistent with the inference. All of these excellent properties were inseparable from the material itself; the three-dimensional microstructure provides space for the reaction, a larger surface area provided an area for surface adsorption, and mesopores also promote the sodium ion. The most important thing was that the large interlayer spacing reduces the resistance of sodium ions to intercalation and deintercalation. In summary, it provided the ideas for other types of energy storage systems because of the low production cost and simple preparation process.

ASSOCIATED CONTENT

Supporting Information

The Supporting Information is available free of charge on the ACS Publications website at DOI: 10.1021/acsami.8b13160.

XRD pattern of CPP; Raman pattern of CPP; nitrogen adsorption−desorption isotherms and BJH pore size distributions of CPP, the inset figure is a partial enlargement of the pore size distribution of 2−14 nm; elemental ratio on the surface of CPP; comparison of the rate performance of different biomass-derived carbon materials; electrochemical impedance spectra of the CPP anodes at different cycles and equivalent circuits; and impedance parameters of CPP electrodes (PDF)

AUTHOR INFORMATION

Corresponding Authors

*E-mail: zengxiaoyuan721@126.com (X.Z.).
*E-mail: zyjkmust@126.com (Y.Z.).
*E-mail: xsun9@uwo.ca (X.S.).

ORCID

Xiaoyuan Zeng: 0000-0001-8596-1094

Author Contributions

§Y.Z. and X.L. authors contributed equally to this work.

Notes

The authors declare no competing financial interest.

ACKNOWLEDGMENTS

This work is supported by the National Natural Science Foundation of China (NSFC project no. 51604132, 51404120, and 51764029) and the Applied Basic Research Plan of Yunnan Province (nos. 2017FD091 and 2017FB085).

REFERENCES

(1) Bruce, P. G.; Freunberger, S. A.; Hardwick, L. J.; Tarascon, J.-M. $LigO_2$ and LigS batteries with high energy storage. *Nat. Mater.* **2012**, *11*, 19−29.
(2) Yabuuchi, N.; Kubota, K.; Dahbi, M.; Komaba, S. Research development on sodium-ion batteries. *Chem. Rev.* **2014**, *114*, 11636−11682.
(3) Armand, M.; Tarascon, J.-M. Building better batteries. *Nature* **2008**, *451*, 652−657.
(4) Chen, X.; Luo, C.; Zhang, J.; Kong, J.; Zhou, T. Sustainable Recovery of Metals from Spent Lithium-Ion Batteries: A Green Process. *ACS Sustainable Chem. Eng.* **2015**, *3*, 3104.
(5) Tian, X. L.; Xu, Y. Y.; Zhang, W.; Wu, T.; Xia, B. Y.; Wang, X. Unsupported Platinum-Based Electrocatalysts for Oxygen Reduction Reaction. *ACS Energy Lett.* **2017**, *2*, 2035−2043.
(6) Pan, J.; Xu, Y. Y.; Yang, H.; Dong, Z.; Liu, H.; Xia, B. Y. Advanced Architectures and Relatives of Air Electrodes in Zn-Air Batteries. *Adv. Sci.* **2018**, *5*, 1700691.
(7) Winter, M.; Brodd, R. J. What Are Batteries, Fuel Cells, and Supercapacitors? *Chem. Rev.* **2005**, *105*, 1021.
(8) Slater, M. D.; Kim, D.; Lee, E.; Johnson, C. S. Sodium-Ion Batteries. *Adv. Funct. Mater.* **2013**, *23*, 947−958.
(9) Kundu, D.; Talaie, E.; Duffort, V.; Nazar, L. F. The Emerging Chemistry of Sodium Ion Batteries for Electrochemical Energy Storage. *Angew. Chem. Int. Ed.* **2015**, *54*, 3431−3448.
(10) Zhang, Y.; Li, X.; Zhang, M.; Liao, S.; Dong, P.; Xiao, J.; Zhang, Y.; Zeng, X. IrO_2 nanoparticles highly dispersed on nitrogen-doped carbon nanotubes as an efficient cathode catalyst for high-performance Li-O_2 batteries. *Ceram. Int.* **2017**, *43*, 14082−14089.
(11) Dang, D.; Zou, H.; Xiong, Z.; Hou, S.; Shu, T.; Nan, H.; Zeng, X.; Zeng, J.; Liao, S. High-Performance, Ultralow Platinum Membrane Electrode Assembly Fabricated by In Situ Deposition of a Pt Shell Layer on Carbon-Supported Pd Nanoparticles in the Catalyst Layer Using a Facile Pulse Electrodeposition Approach. *ACS Catal.* **2015**, *5*, 4318−4324.
(12) Wang, L. P.; Yu, L.; Wang, X.; Srinivasan, M.; Xu, Z. J. Recent developments in electrode materials for sodium-ion batteries. *J. Mater. Chem. A* **2015**, *3*, 9353−9378.
(13) Hwang, J.; Myung, S.-T.; Sun, Y.-K. Sodium-ion batteries: present and future. *Chem. Soc. Rev.* **2017**, *46*, 3529.
(14) Kim, S.-W.; Seo, D.-H.; Ma, X.; Ceder, G.; Kang, K. Electrode Materials for Rechargeable Sodium-Ion Batteries: Potential Alternatives to Current Lithium-Ion Batteries. *Adv. Energy Mater.* **2012**, *2*, 710−721.
(15) Pan, H.; Hu, Y.-S.; Chen, L. Room-temperature stationary sodium-ion batteries for large-scale electric energy storage. *Energy Environ. Sci.* **2013**, *6*, 2338.
(16) Yang, Z.; Zhang, J.; Kintner-Meyer, M. C. W.; Lu, X.; Choi, D.; Lemmon, J. P.; Liu, J. Electrochemical energy storage for green grid. *Chem. Rev.* **2011**, *111*, 3577−3613.
(17) Wang, H.-g.; Wu, Z.; Meng, F.-l.; Ma, D.-l.; Huang, X.-l.; Wang, L.-m.; Zhang, X.-b. Nitrogen-Doped Porous Carbon Nanosheets as Low-Cost, High-Performance Anode Material for Sodium-Ion Batteries. *Chemsuschem* **2013**, *6*, 56−60.
(18) DiVincenzo, D. P.; Mele, E. J. Cohesion and structure in stage-1 graphite intercalation compounds. *Phys. Rev. B: Condens. Matter Mater. Phys.* **1985**, *32*, 2538−2553.
(19) GE, P.; Fouletier, M. Electrochemical intercalation of sodium in graphite. *Solid State Ionics* **1988**, *28-30*, 1172−1175.
(20) Komaba, S.; Murata, W.; Ishikawa, T.; Yabuuchi, N.; Ozeki, T.; Nakayama, T.; Ogata, A.; Gotoh, K.; Fujiwara, K. Electrochemical Na Insertion and Solid Electrolyte Interphase for Hard-Carbon Electrodes and Application to Na-Ion Batteries. *Adv. Funct. Mater.* **2011**, *21*, 3859−3867.
(21) Chen, W.; Deng, D. Deflated Carbon Nanospheres Encapsulating Tin Cores Decorated on Layered 3-D Carbon

DOI: 10.1021/acsami.8b13160
ACS Appl. Mater. Interfaces 2018, 10, 42796−42803

Structures for Low-Cost Sodium Ion Batteries. *ACS Sustainable Chem. Eng.* **2015**, *3*, 63−70.
(22) Hameed, A. S.; Reddy, M. V.; Chen, J. L. T.; Chowdari, B. V. R.; Vittal, J. J. RGO/Stibnite Nanocomposites as Dual Anode for Lithium and Sodium Ion Batteries. *ACS Sustainable Chem. Eng.* **2016**, *4*, 2479.
(23) Alcántara, R.; Madrigal, F. J. F.; Lavela, P.; Tirado, J. L.; Mateos, J. M. J.; de Salazar, C. G.; Stoyanova, R.; Zhecheva, E. Characterisation of mesocarbon microbeads (MCMB) as active electrode material in lithium and sodium cells. *Carbon* **2000**, *38*, 1031−1041.
(24) Wang, Y.; Feng, Z.; Zhu, W.; Gariépy, V.; Gagnon, C.; Provencher, M.; Laul, D.; Veillette, R.; Trudeau, M.; Guerfi, A.; Zaghib, K. High Capacity and High Efficiency Maple Tree-Biomass-Derived Hard Carbon as an Anode Material for Sodium-Ion Batteries. *Materials* **2018**, *11*, 1294.
(25) Wang, S.; Wang, W.; Zhan, P.; Yuan, Y.; Jiao, K.; Jiao, H.; Jiao, S. 3D flower-like NaHTi3O7 nanotubes as high-performance anodes for sodium-ion batteries. *J. Mater. Chem. A* **2015**, *3*, 16528−16534.
(26) Jiang, L.; Sheng, L.; Fan, Z. Biomass-derived carbon materials with structural diversities and their applications in energy storage. *Sci. China Mater.* **2017**, *61*, 133.
(27) Kim, K.; Lim, D. G.; Han, C. W.; Osswald, S.; Ortalan, V.; Youngblood, J. P.; Pol, V. G. Tailored Carbon Anodes Derived from Biomass for Sodium-Ion Storage. *ACS Sustainable Chem. Eng.* **2017**, *5*, 8720−8728.
(28) Wang, H.; Yu, W.; Shi, J.; Mao, N.; Chen, S.; Liu, W. Biomass derived hierarchical porous carbons as high-performance anodes for sodium-ion batteries. *Electrochim. Acta* **2016**, *188*, 103−110.
(29) Zhou, X.; Lu, X.; Zhang, Z.; Lu, H.; Lei, Z. Xanthoceras sorbifolia husks-derived porous carbon for sodium-ion and lithium-sulfur batteries. *Diam. Relat. Mater.* **2018**, *85*, 104−111.
(30) Wang, P.; Li, X.; Li, X.; Shan, H.; Li, D.; Sun, X. Paulownia tomentosa derived porous carbon with enhanced sodium Storage. *J. Mater. Res.* **2018**, *33*, 1236.
(31) Zhu, H.; Jia, Z.; Chen, Y.; Weadock, N.; Wan, J.; Vaaland, O.; Han, X.; Li, T.; Hu, L. Tin anode for sodium-ion batteries using natural wood fiber as a mechanical buffer and electrolyte reservoir. *Nano Lett.* **2013**, *13*, 3093−3100.
(32) Irisarri, E.; Ponrouch, A.; Palacin, M. R. Review-Hard Carbon Negative Electrode Materials for Sodium-Ion Batteries. *J. Electrochem. Soc.* **2015**, *162*, A2476−A2482.
(33) Wang, H.; Yu, W.; Shi, J.; Mao, N.; Chen, S.; Liu, W. Biomass derived hierarchical porous carbons as high-performance anodes for sodium-ion batteries. *Electrochim. Acta* **2016**, *188*, 103−110.
(34) Cao, L.; Hui, W.; Xu, Z.; Huang, J.; Zheng, P.; Li, J.; Sun, Q. Rape seed shuck derived-lamellar hard carbon as anodes for sodium-ion batteries. *J. Alloys Compd.* **2017**, *695*, 632−637.
(35) Zhu, Z.; Liang, F.; Zhou, Z.; Zeng, X.; Wang, D.; Dong, P.; Zhao, J.; Sun, S.; Zhang, Y.; Li, X. Expanded biomass-derived hard carbon with ultra-stable performance for sodium-ion batteries. *J. Mater. Chem. A* **2018**, *6*, 1513.
(36) Lotfabad, E. M.; Ding, J.; Cui, K.; Kohandehghan, A.; Kalisvaart, W.; Hazelton, M.; Mitlin, D. High-Density Sodium and Lithium Ion Battery Anodes from Banana Peels. *ACS Nano* **2015**, *8*, 7115.
(37) Wu, L.; Buchholz, D.; Vaalma, C.; Giffin, G. A.; Passerini, S. Apple-Biowaste-Derived Hard Carbon as a Powerful Anode Material for Na-Ion Batteries. *ChemElectroChem* **2016**, *3*, 292.
(38) Li, H.; Shen, F.; Luo, W.; Dai, J.; Han, X.; Chen, Y.; Yao, Y.; Fu, K.; Zhu, H.; Hitz, E. M. Carbonized leaf membrane with anisotropic surfaces for sodium ion battery. *ACS Appl. Mater. Interfaces* **2016**, *8*, 2204.
(39) Wen, Y.; He, K.; Zhu, Y.; Han, F.; Xu, Y.; Matsuda, I.; Ishii, Y.; Cumings, J.; Wang, C. Expanded graphite as superior anode for sodium-ion batteries. *Nat. Commun.* **2014**, *5*, 4033.
(40) Liu, Y.; Zhang, N.; Yu, C.; Jiao, L.; Chen, J. $MnFe_2O_4$@C Nanofibers as High-Performance Anode for Sodium-Ion Batteries. *Nano Lett.* **2016**, *16*, 3321−3328.
(41) Qiu, S.; Xiao, L.; Sushko, M. L.; Han, K. S.; Shao, Y.; Yan, M.; Liang, X.; Mai, L.; Feng, J.; Cao, Y.; Ai, X.; Yang, H.; Liu, J. Manipulating Adsorption-Insertion Mechanisms in Nanostructured Carbon Materials for High-Efficiency Sodium Ion Storage. *Adv. Funct. Mater.* **2017**, *7*, 1700403.
(42) Yang, D.; Velamakanni, A.; Bozoklu, G.; Park, S.; Stoller, M.; Piner, R. D.; Stankovich, S.; Jung, I.; Field, D. A.; Ventrice, C. A.; Ruoff, R. S. Chemical analysis of graphene oxide films after heat and chemical treatments by X-ray photoelectron and Micro-Raman spectroscopy. *Carbon* **2009**, *47*, 145−152.
(43) Ou, J.; Yang, L.; Zhang, Z.; Xi, X. Nitrogen-doped porous carbon derived from horn as an advanced anode material for sodium ion batteries. *Microporous Mesoporous Mater.* **2017**, *237*, 23−30.
(44) Zhang, F.; Yao, Y.; Wan, J.; Henderson, D.; Zhang, X.; Hu, L. High Temperature Carbonized Grass as a High Performance Sodium Ion Battery Anode. *ACS Appl. Mater. Interfaces* **2016**, *9*, 391−397.
(45) Hou, H.; Banks, C. E.; Jing, M.; Zhang, Y.; Ji, X. Carbon Quantum Dots and Their Derivative 3D Porous Carbon Frameworks for Sodium-Ion Batteries with Ultralong Cycle Life. *Adv. Mater.* **2015**, *27*, 7861−7866.
(46) Chen, T.; Liu, Y.; Pan, L.; Lu, T.; Yao, Y.; Sun, Z.; Chua, D. H. C.; Chen, Q. Electrospun carbon nanofibers as anode materials for sodium ion batteries with excellent cycle performance. *J. Mater. Chem. A* **2014**, *2*, 4117.
(47) Hong, K.-l.; Qie, L.; Zeng, R.; Yi, Z.-q.; Zhang, W.; Wang, D.; Yin, W.; Wu, C.; Fan, Q.-j.; Zhang, W.-x.; Huang, Y.-h. Biomass derived hard carbon used as a high performance anode material for sodium ion batteries. *J. Mater. Chem. A* **2014**, *2*, 12733.
(48) Jin, J.; Yu, B.-j.; Shi, Z.-q.; Wang, C.-y.; Chong, C.-b. Lignin-based electrospun carbon nanofibrous webs as free-standing and binder-free electrodes for sodium ion batteries. *J. Power Sources* **2014**, *272*, 800−807.
(49) Luo, W.; Bommier, C.; Jian, Z.; Li, X.; Carter, R.; Vail, S.; Lu, Y.; Lee, J.-J.; Ji, X. Low-surface-area hard carbon anode for na-ion batteries via graphene oxide as a dehydration agent. *ACS Appl. Mater. Interfaces* **2015**, *7*, 2626−2631.
(50) Liu, H.; Jia, M.; Sun, N.; Cao, B.; Chen, R.; Zhu, Q.; Wu, F.; Qiao, N.; Xu, B. Nitrogen-Rich Mesoporous Carbon as Anode Material for High-Performance Sodium-Ion Batteries. *ACS Appl. Mater. Interfaces* **2015**, *7*, 27124−27130.
(51) Wang, C.; Huang, J.; Qi, H.; Cao, L.; Xu, Z.; Cheng, Y.; Zhao, X.; Li, J. Controlling pseudographtic domain dimension of dandelion derived biomass carbon for excellent sodium-ion storage. *J. Power Sources* **2017**, *358*, 85−92.
(52) Tang, K.; Fu, L.; White, R. J.; Yu, L.; Titirici, M.-M.; Antonietti, M.; Maier, J. Hollow Carbon Nanospheres with Superior Rate Capability for Sodium-Based Batteries. *Adv. Energy Mater.* **2012**, *2*, 873−877.
(53) Ding, J.; Wang, H.; Li, Z.; Kohandehghan, A.; Cui, K.; Xu, Z.; Zahiri, B.; Tan, X.; Lotfabad, E. M.; Olsen, B. C.; Mitlin, D. Carbon nanosheet frameworks derived from peat moss as high performance sodium ion battery anodes. *ACS Nano* **2013**, *7*, 11004−11015.
(54) Augustyn, V.; Come, J.; Lowe, M. A.; Kim, J. W.; Taberna, P.-L.; Tolbert, S. H.; Abruña, H. D.; Simon, P.; Dunn, B. High-rate electrochemical energy storage through Li^+ intercalation pseudocapacitance. *Nat. Mater.* **2013**, *12*, 518−522.
(55) Wang, J.; Polleux, J.; Lim, J.; Dunn, B. Pseudocapacitive contributions to electrochemical energy storage in TiO_2 (anatase) nanoparticles. *J. Phys. Chem. C* **2007**, *111*, 14925−14931.
(56) Bommier, C.; Surta, T. W.; Dolgos, M.; Ji, X. New Mechanistic Insights on Na-Ion Storage in Nongraphitizable Carbon. *Nano Lett.* **2015**, *15*, 5888−5892.
(57) Li, Y.; Hu, Y.-S.; Qi, X.; Rong, X.; Li, H.; Huang, X.; Chen, L. Advanced sodium-ion batteries using superior low cost pyrolyzed anthracite anode: towards practical applications. *Energy Storage Mater.* **2016**, *5*, 191.
(58) Li, Y.; Hu, Y.-S.; Titirici, M.-M.; Chen, L.; Huang, X. Hard Carbon Microtubes Made from Renewable Cotton as High-

DOI: 10.1021/acsami.8b13160
ACS Appl. Mater. Interfaces 2018, 10, 42796−42803

Performance Anode Material for Sodium-Ion Batteries. *Adv. Energy Mater.* **2016**, *6*, 1600659.
(59) Xiao, L.; Cao, Y.; Henderson, W. A.; Sushko, M. L.; Shao, Y.; Xiao, J.; Wang, W.; Engelhard, M. H.; Nie, Z.; Liu, J. Hard carbon nanoparticles as high-capacity, high-stability anodic materials for Na-ion batteries. *Nano Energy* **2016**, *19*, 279−288.
(60) Wang, Q.; Zhu, X.; Liu, Y.; Fang, Y.; Zhou, X.; Bao, J. Rice husk-derived hard carbons as high-performance anode materials for sodium-ion batteries. *Carbon* **2017**, *127*, 658.

DOI: 10.1021/acsami.8b13160
ACS Appl. Mater. Interfaces 2018, 10, 42796−42803